Corresponding author: V.V. Atuchin
Institute of Semiconductor Physics, Novosibirsk 630090, Russia
Phone: +7 (383) 3308889
E-mail: atuchin@isp.nsc.ru

Synthesis, structural and spectroscopic properties of orthorhombic compounds $BaLnCuS_3$ (Ln = Pr, Sm)

Nikita O. Azarapin[1], Aleksandr S. Aleksandrovsky[2,3], Victor V. Atuchin[4,5,6], Tatyana A. Gavrilova[7], Aleksandr S. Krylov[8], Maxim S. Molokeev[9,10,11], Shaibal Mukherjee[12], Aleksandr S. Oreshonkov[8,11], Oleg V. Andreev[1]

[1]Institute of Chemistry, Tyumen State University, Tyumen 625003, Russia

[2]Laboratory of Coherent Optics, Kirensky Institute of Physics Federal Research Center KSC SB RAS, Krasnoyarsk 660036, Russia

[3]Department of Photonics and Laser Technologies, Siberian Federal University, Krasnoyarsk 660041, Russia

[4]Laboratory of Optical Materials and Structures, Institute of Semiconductor Physics, SB RAS, Novosibirsk 630090, Russia

[5]Functional Electronics Laboratory, Tomsk State University, Tomsk 634050, Russia

[6]Research and Development Department, Kemerovo State University, Kemerovo 650000, Russia

[7]Laboratory of Nanodiagnostics and Nanolithography, Institute of Semiconductor Physics, SB RAS, Novosibirsk 630090, Russia

[8]Laboratory of Molecular Spectroscopy, Kirensky Institute of Physics Federal Research Center KSC SB RAS, Krasnoyarsk 660036, Russia

[9]Laboratory of Crystal Physics, Kirensky Institute of Physics Federal Research Center KSC SB RAS, Krasnoyarsk 660036, Russia

[10]Department of Physics, Far Eastern State Transport University, Khabarovsk 680021, Russia

[11]Siberian Federal University, Krasnoyarsk 660079, Russia

[12]Hybrid Nanodevice Research Group (HNRG), Electrical Engineering, Indian Institute of Technology Indore, Madhya Pradesh 453552, India

Abstract

Ternary sulfides $BaPrCuS_3$ and $BaSmCuS_3$ are first synthesized by the sulphidation reaction of a mixture of related oxides and metal Cu in a flow of (CS_2, H_2S) at 1170 K. The crystal structures of $BaPrCuS_3$ and $BaSmCuS_3$ are obtained by Rietveld method. $BaPrCuS_3$ crystallizes in space group *Pnma* with unit cell parameters a = 10.56074(6), b = 4.11305(2) and c = 13.42845(7) Å, V = 583.289 (5) $Å^3$, Z = 2. $BaSmCuS_3$ crystallizes in space group *Cmcm* with unit cell parameters a = 4.07269(4), b = 13.4499(1) and c = 10.3704(1) Å, V = 568.06 (1) $Å^3$, Z = 2. The structural model is proposed for the *Cmcm*→*Pnma* transition in compounds $ABCX_3$ (X = S, Se) for the sequence Sm-Pm-Nd-Pr. The dimensionless tolerance factor $t = IR(A)\times IR(C)/IR(B)^2$ is suggested to control the boundary between the *Cmcm* and *Pnma* structures. The micromorphological, thermal and spectroscopic properties are evaluated for $BaPrCuS_3$. The compound melts incongruently at T_{melt} = 1580.9 K. In $BaPrCuS_3$, the band gap is estimated to be 2.1 eV. The vibrational parameters of $BaPrCuS_3$ and $BaSmCuS_3$ are comparatively observed by Raman spectroscopy.

Keywords: Complex sulfides, Crystal structure, SEM, Raman.

1. Introduction

Complex chalcogenide compounds have interesting chemical and physical properties and the materials are widely used in modern optical and electronic technologies [1-10]. In recent years, complex Cu^+-containing sulfides and selenides were considered as promising thin film absorber materials in solar cell structures [11-16]. This activated general interest to crystal chemistry and the properties of Cu^+ chalcogenides, including a search for new materials. In particular, the compounds

with generalized composition $ABCX_3$, where A –alkaline-earth metal, B – d- or f-element, C – other d-element, X – chalcogenide, can be considered [1]. Earlier, besides crystal structures, the semiconductor, magnetic, optical and thermodynamic properties were reported on for the selected compounds from this family [1,17-25]. Besides, several compounds $Eu^{2+}BC'S_3$ have been recently discovered [7,26-28]. It is known that compounds $ABCX_3$ can crystallize in seven structural types: $KZrCuS_3$ (*Cmcm*), Eu_2CuS_3 (*Pnma*), Ba_2MnS_3 (*Pnma*), $BaCuLaS_3$ (*Pnma*), $BaAgErS_3$ (*C*2/*m*), $NaCuTiS_3$ (*Pnma*), $TlCuTiTe_3$ (*P*2$_1$/*m*) [1]. Among these crystals, the $ALnCuQ_3$ compounds are particularly interesting because Ln elements possess rich crystal chemistry and specific spectroscopic properties.

The known $ALnCuS_3$ compounds crystallize in Eu_2CuS_3 (*Pnma*) or $KZrCuS_3$ (*Cmcm*) structural types and the rules governing the relation between the element composition and structure type was not defined for this ternary sulfide family [1]. The crystal structures related to these structural types are very similar. The structures are formed by layers of CuX_4 tetrahedra and LnX_6 octahedra [29,30]. The present study is aimed at the synthesis and evaluation of compounds $BaPrCuS_3$ and $BaSmCuS_3$ as the representative members of $ALnCuS_3$ sulfides. The compounds were not observed earlier. As to other $BaLnCuS_3$ sulfides, several compounds were synthesized in the past for Ln= La, Ce, Nd, Er, Sc, Y, and the structures were defined for $BaLaCuS_3$ (*Pnma*) and $BaErCuS_3$ (*Cmcm*) [17,18]. Also, the space groups *Pnma* and *Cmcm* were adopted for Ln = Ce, Nd and Ln = Sc, Y, Gd, respectively. Thus, the phase transition appears on the rare-earth element substitution in $BaLnCuS_3$ structures. The formation of $BaCuLnS_3$ (Ln = Pr, Sm) is assumed in the quasithreefold BaS-Ln_2S_3-Cu_2S systems. It should be mentioned that the BaS-Ln_2S_3-Cu_2S phase diagram has not been defined yet for Ln = Pr, Sm. The known analogous systems $(Ba,Sr,Eu^{2+})S$-Ln_2S_3-Cu_2S have the composite equilibriums including peritectic/eutectic interactions and extensive ranges of solid solutions [22,23,28,31,32] and, respectively, the synthesis of $BaPrCuS_3$ and $BaSmCuS_3$ seems to be not trivial. In the present experiment, the sulfides are prepared by the sulphidation method and final

powder products are observed by conventional experimental techniques to see their structural, morphological and vibrational characteristics.

2. Experimental section

Syntheses. $BaPrCuS_3$ and $BaSmCuS_3$ compounds were prepared in powder forms by the sulphidation of oxide mixtures received after the decomposition of metal nitrate solutions. In the synthesis, for better comparison, the key steps were the same for both compounds of barium, rare-earth element and copper.

The high purity starting reagents were used: Cu (99,9%, SZB Tsvetmet, Russia), $BaCO_3$ (99,99%, ultrapure, KAI YONG, China), Pr_6O_{11} (99,99%, ultrapure, TDM-96 Ltd. Russia), Sm_2O_3 (99,99%, ultrapure, TDM-96 Ltd. Russia) and concentrated nitric acid solution ($C(HNO_3)$ = 14.6 mol/l, ultrapure, Vekton Ltd., Russia). Ammonium rodanide NH_4SCN (98%, Vekton Ltd., Russia). Weighing them was carried out on the assay balances of Mettler Toledo with the accuracy of 0.1 mg. Before weighing, a copper plate of ~1 mm in thickness was etched in the $HClO_3$ solution to remove the surface oxide and was washed out in distilled water. Then, the Cu plate was cut into segments of ~1-5 mm^2 in area. All starting metal oxides were calcinated in quartz crucibles at 1300 K for 5 h in the air to remove surface adsorbates and decompose the hydrocarbonates commonly present on the rare-earth oxide surface. The acid solutions were measured by means of glass measuring graduates with the accuracy of 0.1 ml.

For the synthesis of $BaPrCuS_3$, the starting reagents were taken at the stoichiometric molar ratio 6Cu: Pr_6O_{11}: 6$BaCO_3$ (Cu – 0.8151 g, Pr_6O_{11} – 2.1866 g, $BaCO_3$ – 2.5289 g). For $BaSmCuS_3$, the starting reagents were taken at the stoichiometric molar ratio 2Cu:Sm_2O_3:2$BaCO_3$ (Cu – 0.7967 g, Sm_2O_3 – 2.1832 g, $BaCO_3$ – 2.4718 g). The charge was inserted in a heat-resistant flat-bottom beaker and, then, concentrated HNO_3 10 ml (~21% excess) was added. For the best dissolution, the mixture was warmed up on a laboratory tile for the total disappearance of solid components. The solutions of initial nitrates were formed by reactions:

$$6BaCO_3 + Pr_6O_{11} + 6Cu + 54HNO_3 \rightarrow 6Ba(NO_3)_2 + 6Pr(NO_3)_3 + 6CuNO_3 + 27H_2O + 12NO_2\uparrow + 6CO_2\uparrow + 4O_2\uparrow$$

$$2BaCO_3 + Sm_2O_3 + 2Cu + 18HNO_3 \rightarrow 2Ba(NO_3)_2 + 2Sm(NO_3)_3 + 2CuNO_3 + 9H_2O + 4NO_2\uparrow + 2CO_2\uparrow$$

Then, the temperature was increased to 500-600 K and the solution was evaporated up to the formation of a solid. On the heating, the solution color changed from blue to green and the brown gas (NO_2) appeared. That indicates the formation of a compound or a complex on the basis of Cu. The high temperature was kept up to the evaporation of all volatile components. As a result of this treatment, a black color cake was formed. After the evaporation stage, the beaker was cooled and the cake was extracted. Then, the solid cake was ground in an agate mortar. The powder was inserted in a fuzzed quartz boat and treated in the muffle furnace at 1170 K until the end of residual brown gas extraction. After this moment, the sample was calcinated at 1170 K for 2 h in the air. After the annealing, the quartz boat was cooled to room temperature and the final product was ground in an agate mortar. As a result, the stoichiometric oxide mixture was formed.

The sulphidation process was carried out in a vertical quartz reactor at the temperature of 1270 K. The oxide charge was placed in a silica container and inserted in the reactor. Then the reactor was heated to 1270 K and filled with a mixture of argon and sulfiding gas CS_2/H_2S generated by the decomposition of ammonium thiocyanate NH_4CSN [33]. For each substance, the reaction was conducted for 5 h:

$$2BaO + Ln_2O_3 + Cu_2O + 3CS_2 \rightarrow 2BaLnCuS_3 + 3CO_2$$

The final powder products of $BaLnCuS_3$ were of flavovirent color, as shown in Figure 1. As it appears, the color similarity of the compounds is dominated by the presence of Cu^+. The following advantages of this synthesis route could be mentioned:

- Sedimentation from the nitrate solution allows for the sample homogenization that reduces the time needed for the synthesis of oxide precursor and increases the final product yield.
- Less time needed for the synthesis of sulfide compound in comparison with that typical of ampule synthesis methods.
- Oxide precursors stable at normal conditions are used in the sulfide synthesis.

Characterization. The powder diffraction data of $BaLnCuS_3$ for Rietveld analysis were collected at room temperature with a Bruker D8 ADVANCE powder diffractometer (Cu-Kα radiation) and linear VANTEC detector. The step size of 2θ was 0.016°. The 2θ range of 10-70º was measured with a 0.6 mm divergence slit and the counting time was 7 s per step, but the 2θ range of 70-150º was measured with a 2 mm divergence slit and 12 sec per step. Larger slits allow for a noticeable increase of the intensity of high-angle peaks without a loss of resolution because the high-angle peaks are broad enough to be not affected by a bigger divergence beam. The esd's $\sigma(I_i)$ of all points on the patterns were calculated using intensities I_i: $\sigma(I_i)=I_i^{1/2}$. The intensities and obtained esd's were further normalized: $I_{i\ norm} = I_i \times 0.6 \times 7/(\text{slit width} \times \text{time per step})$, $\sigma_{norm}(I_i) = \sigma(I_i) \times 0.6 \times 7/(\text{slit width} \times \text{time per step})$, taking into account the actual divergence slit width value, which was used to measure each particular intensity I_i, and saved in the xye-type file. So, the transformed powder pattern has a usual view in the whole 2θ range of 5-150º, but all high-angle points have small esd values.

The optical absorption measurements were carried out for powder samples using a UV-2600 Series Shimadzu spectrometer. The UV-visible spectra were recorded over the wavelength range of 190-1400 nm at room temperature. The particle micromorphology was observed by SEM using a LEO 1430 device. The Raman spectra were collected in backscattering geometry using a triple Raman spectrometer Jobin Yvon T64000 operating in double subtractive mode. The spectra were detected by a liquid nitrogen-cooled CCD cooled to 140 K. The spectral resolution for the recorded Stokes side Raman spectra was about 1 cm^{-1} (this resolution was achieved by using gratings with

1800 grooves mm^{-1} and 100 μm slits). The deformation of the low-frequency spectral edge by an optical slit, which sometimes smears the right features of the low-frequency spectra, was carefully eliminated by rigorous optical alignment. Raman spectra of $BaPrCuS_3$ were recorded at the 514.5 nm excitation wavelength from Spectra Physics Stabilite 2017 laser. To avoid possible excitation of the luminescence of Sm^{3+} ion at the transition to $^4F_{3/2}$ in case of the excitation source specified above, the 647.1 nm line of Lexel 95K laser at 100 mW power (5 mW on the sample) was used as an excitation light source for Raman spectroscopy of $BaSmCuS_3$.

The simultaneous thermal analysis was performed in the He (99,999%, Russia) flow with use of a STA 449 F3 Jupiter instrument equipped with a (W3%Re – W25%Re) thermocouple. The analyzed powder sample weighed (90-100)±0.01 mg. The temperature adjustment accuracy was not above 0.3 K. In the temperature range, where thermal events were observed, the heating rate was 10 K/min. The results of DSK/TG experiments were processed in the Proteus-6 programs package [34]. The possible error in the phase transition enthalpy determination was ±18%.

3. Results and discussion

Rietveld refinement was performed using TOPAS 4.2 [35] which accounts the esd's of each point by a special weight scheme. All peaks measured for $BaPrCuS_3$ were indexed by an orthorhombic unit cell (space group *Pnma*) with cell parameters close to those of $BaNdCuS_3$ [18]. However, $BaSmCuS_3$ peaks were indexed by an orthorhombic cell (space group *Cmcm*) with parameters close to those of $KThCuS_3$ [36]. Besides, in this sample, a small amount (~5% wt.) of $BaCu_2S_2$ (space group *Pnma*) [37] impurity was detected. These crystal structures were taken as the starting models for Rietveld refinements.

In order to obtain the model of $BaPrCuS_3$, the Nd^{3+} site in $BaNdCuS_3$ was assumed to be occupied by the Pr^{3+} ion. To obtain the $BaSmCuS_3$ model, the K^+ site in $KThCuS_3$ was replaced by Ba, and Th^{4+} was replaced by Sm^{3+}. The thermal parameters of Ba^{2+}, Pr^{3+} and Sm^{3+} ions were refined anisotropically, but Cu^+ and S^{2-} ions were refined with isotropic thermal parameters. The

refinements were stable and gave low *R*-factors (Table 1, Figure 2). The obtained coordinates, main bond lengths and anisotropic thermal parameters are in Table 2, Tables 1S and 2S, respectively. The crystal structures of $BaPrCuS_3$ and $BaSmCuS_3$ are presented in Figure 3. Further details of the crystal structures may be obtained from Fachinformationszentrum Karlsruhe, 76344 Eggenstein-Leopoldshafen, Germany (fax: (+49)7247-808-666; E-mail: crystdata@fiz-karlsruhe.de; http://www.fiz-karlsruhe.de/request_for_deposited_data.html on quoting the deposition numbers CSD-1948871 and 1948872.

Thus, two different structures are observed in $BaLnCuS_3$ compounds for the sequence Sm-Pm-Nd-Pr. On the one hand, $BaSmCuS_3$ crystallizes in space group *Cmcm*, and, on the other hand, $BaNdCuS_3$ and $BaPrCuS_3$ crystallize in space group *Pnma*. The $BaPmCuS_3$ structure remains unknown. Accordingly, it is valuable to define the relation governing the structure type in $ABCX_3$ crystals. In order to make the space group prediction for the compounds with general formula $ABCX_3$, it was decided to consider the structures known for X = S, Se from the ICSD database. Generally, the structure consists of AX_7, BX_7 and CX_4 polyhedra columns parallel to the *b*-axis, and they join each other by edges, as shown in Figure S1. The crystal structure deformation and the change of the corresponding space group should depend on ion radii IR(A), IR(B), IR(C) because the column lengths directly depend on them. As it can be reasonably assumed, anion ion radii IR(X) should lead to the overall cell volume deformation without a drastic change of a structure and a space group should not depend on this factor. It is valuable to find the tolerance factor *t*(IR(A),IR(B),IR(C)), which controls the space group. But the function is not clear. To solve this problem, a deep learning model with three input neurons IR(A), IR(B), IR(C), two intermediate layers with two neurons and one output neuron was built in package Python 3.6 [38]. The conventional sigmoid activation function was used for all layers. In the model, the output neuron with the 0 value means space group *Pnma*, but 1 means the *Cmcm* group. About 2000 epochs of learning were launched and, finally, the small loss function of 5.2% was reached with a high accuracy. The first weight matrix revealed that weights associated with IR(A), IR(C) neurons are

big and positive in the range of 1.3-2. The weights associated with IR(B) are also big, but negative, and the weight values are in the range from −3.4 to −3.0. Therefore, we can conclude that the tolerance factor should proportionally depend on IR(A) and IR(C) values and in the inverse ratio - on IR(B). Moreover, it was found that weights corresponding to the IR(X) neuron are small, and it is in the range of 0.3-0.4. One can really conclude that the output neuron value, i.e. space group, almost does not depend on IR(X). In addition, as seen in Table 3S [39-54], the pair compounds $ABCX_3$ with X = S and X = Se are always crystallized in the same space group. Finally, the dimensionless tolerance factor $t = IR(A)\times IR(C)/IR(B)^2$ was suggested. All $ABCX_3$ (X=S, Se) compounds from ICSD were sorted by increasing the *t* factor and are presented in Table 3S, and the critical value $t = 0.908$ defines the demarcation line between the *Cmcm* and *Pnma* space groups. As shown in Figure 4, all $ABCX_3$ (X=S, Se) compounds can be presented as points in the field defined with two parameters IR(A)*IR(C) and $IR(B)^2$, and the line $t = IR(A)\times IR(C)/IR(B)^2 = 0.908$ cuts the space into two fields with different space groups. Only two compounds $PbYCuS_3$ and $SrYCuSe_3$ (or $PbTbCuS_3$ and $PbDyCuS_3$) positioned in the vicinity to the demarcation line and the rekated points are away from the general trend. First, the structures of these compounds should be investigated more carefully. As for the prediction of the structure type for $BaPmCuS_3$, it seems to be impossible because the related point is assumed to appear on the demarcation line.

The thermal, morphological and spectroscopic properties were measured only for phase-pure $BaPrCuS_3$. As it was shown by the XRD analysis, the available $BaSmCuS_3$ sample contains a significant impurity of $BaCu_2S_2$. Several attempts were made in the synthesis of phase-pure $BaSmCuS_3$ by the sulphidation technique with some variation of the technological parameters. However, in all experiments, the presence of $BaCu_2S_2$ was observed in the final products. The source of this effect is presently unknown, and, accordingly, the synthesis conditions should be optimized to get the phase-pure $BaSmCuS_3$ product.

The $BaPrCuS_3$ powder micromorphology is shown in Figure 5. The powder contains irregular partly agglomerated particles of ~1-5 μm in size. The faceted shapes were not detected and

this may be a result of a drastic anion exchange during the sulpfidation reaction at high temperatures. Under the conditions, the formation of faceted microcrystal shapes seems to be highly improbable. The thermal properties of $BaPrCuS_3$ powder were analyzed over the temperature range from 300 to 1800 K and the related curves are shown in Figure 6. The sample weight was 102.8 mg and the weight loss was not registered in the temperature cycling. The endothermic effect related to the substance melting was observed at T_{melt} = 1580.9 K on heating and the exothermic effect due to the substance crystallization was detected at T_{cryst} = 1607.2 K. Thus, the effect of overcooling is expressed for $BaPrCuS_3$ and the difference between melting and crystallization points is 27 K. The effect of overcooling is bound to the incongruent type of melting. On the heating curve, the melting peak splitting into two components at 1599 K and 1612 K is evident. The heat of melting determined for $BaPrCuS_3$ is equal to ΔH_{melt} = 86.6 kJ·mol^{-1}.

At present, the thermal characteristics of $ALnCuS_3$ compounds are less studied. The thermal parameters available in the literature are summarized in Table 3 [55]. It should be noted that nearly all observed $ALnCuS_3$ compounds melt incongruently. As seen, the melting temperature values obtained for $SrLnCuS_3$ and $EuLnCuS_3$ sulfides are similar for the same Ln element. It is particularly interesting to compare the melting temperatures of the $APrCuS_3$ (A = Sr, Eu, Ba) set. The melting temperature of $BaPrCuS_3$ is noticeably higher than that of $APrCuS_3$ (A = Sr, Eu) and, presumably, this relation indicates a higher thermal stability of the sulfides with bigger radius of the A element. The effect of lanthanide compression can also increase the thermal stability of $ALnCuS_3$ compounds. Indeed, the $BaGdCuS_3$ melts congruently at as high temperature as 1685 K [22] and the temperature is significantly higher than that of $BaPrCuS_3$. The heat of melting obtained for $BaPrCuS_3$ is also noticeably higher than that of $APrCuS_3$ (A = Sr, Eu) and, it is similar to the values known for simple sulfides Ln_2S_3 [56].

To the best of our knowledge, the calculations of the band structures of $BaPrCuS_3$ and $BaSmCuS_3$ are absent in the literature. However, in this situation, the available band structure calculations for monoclinic sulfides $Ba_2Cu_2ThS_5$ and $Ba_2Cu_2US_5$ (space group *C*2/*m*) [57] can be

used for the initial observation of the $BaPrCuS_3$ band structure. Thus, it is reasonably assumed that the valence band top in $BaPrCuS_3$ could formed by S 2p, Cu 3d and Pr 4f orbitals, while the conduction band bottom is formed by the contributions from all ions, including 5d orbitals of Ba and Pr. The strong dependence of the band energy on the direction in Brillouin zone is expected and, therefore, both direct and indirect allowed transitions can contribute to the formation of the fundamental absorption edge.

The Tauc plot, in the case of indirect allowed transitions, for the UV-visible spectra recorded for $BaPrCuS_3$, is shown in Figure 7. The optical bandgap estimated for $BaPrCuS_3$ is equal to 2.1 eV. This value is close to the bandgap value 2.00 eV earlier determined for $BaLaCuS_3$ [17], as well as to the bandgap of another recently studied sulfide $EuErCuS_3$ (1.94 eV) [58]. At the same time, the imperfect linearity of experimental spectrum in the region up to 2.5 eV indicates the contribution of other types of transitions in accordance with the previously formulated assumption. Besides the fundamental absorption band, the minor narrow peak at ~2 eV can be detected in the spectrum and it is ascribed to the *f-f* transition of Pr^{3+} ions, namely, $^3H_4$ -$^1D_2$. Other prominent *f-f* transitions of the Pr^{3+} ion, namely, $^3H_4$-^3P_J (J=0,1,2) and $^1S_0$, cannot be resolved in the obtained spectrum, and, therefore, it should be deduced that the ^3P_J levels of Pr^{3+} are immersed into the conduction band of $BaPrCuS_3$. At the same time, the *f-d* transition of Pr^{3+} ions should be supposed as contributing to the formation of fundamental absorption band.

The emission spectrum obtained from $BaPrCuS_3$ under the excitation at 514.5 nm is shown in Figure S2. The left part of this spectrum in the range below 525 nm is formed by the Raman spectrum with its narrow lines. At the wavelengths above 525 nm, the broad band peaking at 650 nm is observed. This spectral band must be assigned to the luminescence from the conduction band of the electronic structure of $BaPrCuS_3$. The contribution from the *f-f* transitions of the Pr^{3+} ion to the luminescence is obviously absent since the 514.5 nm excitation is inefficient to excite the energy level system of *f* electrons in the Pr^{3+} ion. The luminescence intensity is comparable to that of Raman spectrum. Therefore, $BaPrCuS_3$ is highly likely to be an indirect wide-bandgap

semiconductor, in accordance with the assumption stated above. The energy spacing of spectral replicas observed in the luminescent band is equal to 0.05 eV (400 cm^{-1}). The corresponding vibrational frequencies are absent in the crystal structure of $BaPrCuS_3$. Therefore, the origin of these replicas cannot be ascribed to the well-known phonon replicas in the exciton luminescence and needs a special investigation.

The Raman spectra from $BaPrCuS_3$ and $BaSmCuS_3$ powders are given in Figure 8. For $BaPrCuS_3$, belonging to space group *Pnma*, the mechanical representation at the Brillouin zone (BZ) center can be written as $\Gamma_{vibr} = 12A_g+6A_u + 6B_{1g} + 12B_{1u} + 12B_{2g} + 6B_{2u} + 6B_{3g} + 12B_{3u}$, where the Raman active modes are $\Gamma_{Raman} = 12A_g+6B_{1g} +12B_{2g} + 6B_{3g}$ [59]. The vibrational irreducible representation at the Γ point of BZ for $BaSmCuS_3$ is $\Gamma_{vibr} = 5A_g + 2A_u + 4B_{1g} + 7B_{1u} + B_{2g} + 7B_{2u} + 5B_{3g} + 5B_{3u}$, where Raman active modes are $\Gamma_{Raman} = 5A_g+ 4B_{1g} + B_{2g} + 5B_{3g}$. The difference between the Cu–S1 (Cu–S3) bond lengths in $BaPrCuS_3$ and Cu–S1 in $BaSmCuS_3$ is equal to 0.04 Å; between Cu–S2 bond lengths in $BaPrCuS_3$ and Cu–S2 in $BaSmCuS_3$ is equal to 0.007 Å. Thus, the positions of spectral bands, related to the vibrational modes of CuS_4 tetrahedron, should not differ significantly, but the number of spectral bands should not be the same. The set of Raman spectra in several scattering geometries should be obtained to get the bands related to specified Raman modes. However, in the case of powder samples, such measurements are impossible.

In order to interpret the observed Raman spectra, the calculation of $BaPrCuS_3$ and $BaSmCuS_3$ lattice dynamics using the program package LADY [60] was performed. The atomic vibration values were obtained using the simplified version of Born-Karman model [61]. Within this model, only the pair-wise interactions and bond-stretching force constants F are considered and the model implies that F depends on r_{ij} (interatomic distance). The $F(r_{ij})$ dependences are the same for all atom pairs: $F(r_{ij}) = \lambda\exp(-r_{ij}/\rho)$, where λ and ρ are the parameters characterizing a selected pair interaction. To find the model parameters, a special optimization program was written and tested for several representative compounds [62-68].

As it was noted above, $BaPrCuS_3$ and $BaSmCuS_3$ are members of the $ALnCuS_3$ sulfide family and their structures are formed by the layers of CuS_4 tetrahedra and LnS_6 octahedra [29,30]. According to the lattice dynamics simulations, vibrations at low wavenumbers (20-115 cm^{-1}) are related to the vibration of such layers. For example, the lowest wavenumber Raman-active mode in $BaPrCuS_3$ is graphically shown in Figure 9(a). The strong bands at 62 and 67 cm^{-1} in $BaPrCuS_3$ and $BaSmCuS_3$ are related to the antisymmetric displacements of structural layers, and the vibrations are shown in Figures 9(b) and 9(c), respectively. The difference between $BaPrCuS_3$ and $BaSmCuS_3$ in Raman spectra should be in the range of 115-185 cm^{-1}. There are no trace of Raman-active vibrational modes in this range in the case of $BaSmCuS_3$, but a group of lines is observed in the case of $BaPrCuS_3$ (Figure 8). The region of Raman spectra between 188 and 250 cm^{-1} is related to the vibrations of sulfur ions mainly and, for example, the bending vibration of CuS_4 in $BaSmCuS_3$ is shown in Figure 9(d). It is clearly seen in Figure S1 that CuS_4 tetrahedra from neighboring unit cells share one common vertex and the related vibration of bringing sulfur ion appears in the spectra as a spectral band around 242 cm^{-1} (Figure 9(e)). The stretching-like vibrations in CuS_4 tetrahedra are in the high wavenumber range of 310-350 cm^{-1}, and they are shown in Figure 9(f).

4. Conclusion

This study addresses the synthesis, structure, optical and thermal properties of the new complex sulfides $BaPrCuS_3$ (space group *Pnma*) and $BaSmCuS_3$ (space group *Cmcm*). The compounds crystallize in two different orthorhombic structures that open a possibility to analyze the mechanism of the structure transformation in the known $ABCX_3$ (X = S, Se) compounds for the sequence Sm-Pm-Nd-Pr. To solve this problem, the deep learning neuron model was built on the base of the known $ABCX_3$ compounds. The introduced tolerance factor $t = IR(A)\times IR(C)/IR(B)^2$ can be used as a robust indicator for the prediction of the structure type for compounds $ABCX_3$ (X = S, Se), which crystal structure remains unknown. $BaPrCuS_3$ is shown to be the indirect bandgap compound with bandgap width 2.1 eV.

Acknowledgements

This study was supported by the Russian Science Foundation (19-42-02003). Also, this study was supported by RFBR (18-32-20011, 18-03-00750, in part of Raman analysis). This work is partially supported by DST-RSF project under India-Russia Programme of Cooperation in Science and Technology (No. DST/INT/RUS/RSF/P-20 dated May 16, 2019). Shaibal Mukherjee would like to thank Ministry of Electronics and Information Technology (MeitY) for the Young Faculty Research Fellowship (YFRF) under Visvesvaraya Ph.D. Scheme for Electronics and IT. This publication is an outcome of the R&D work undertaken in the project under the Visvesvaraya Ph.D. Scheme of MeitY being implemented by Digital India Corporation (formerly Media Lab Asia).

References

1. Lukasz A. Koscielski, James A. Ibers, The structural chemistry of quaternary chalcogenides of the type AMM'Q3, Z. Anorg. Allg. Chem. 638 (15) (2012) 2585-2593.
2. Claudia Coughlan, Maria Ibáňez, Oleksandr Dobrozhan, Ajay Singh, Andreu Cabot, Kevin M. Ryan, Compound copper chalcogenide nanocrystals, Chem. Rev. 117 (9) (2017) 5865-6109.
3. Wenlong Yin, Kai Feng, Ran He, Dajiang Mei, Zheshuai Lin, Jiyong Yao, Yicheng Wu, BaGa2MQ6 (M = Si, Ge; Q = S, Se): a new series of promising IR nonlinear optical materials, Dalton Trans. 41 (2012) 5653-5661.
4. Alexander P. Yelisseyev, Marina K. Starikova, Valery V. Korolev, Ludmila I. Isaenko, and Sergey I. Lobanov, Photoluminescence of lithium thiogallate LiGaS2, J. Am. Opt. Soc. B 29 (5) (2012) 1003-1011.
5. A.H. Reshak, I.V. Kityk, O.V. Parasyuk, H. Kamarudin, S. Auluck, Influence of replacing Si by Ge in the chalcogenide quaternary sulfides Ag2In2Si(Ge)S6 on the chemical bonding, linear and nonlinear optical susceptibilities, and hyperpolarizability, J. Phys. Chem. B 117 (8) (2013) 2545-2553.

6. V.V. Atuchin, S.V. Borisov, S.A. Magarill, N.V. Pervukhina, Sphalerite framework in polar sulfides, J. Chem. Crystallogr. 43 (9) (2013) 488-192.
7. Yu.A. Murashko, A.V. Ruseikina, A.A. Kislitsyn, O.V. Andreev, Optical and thermal properties of the EuLnCuS3 (Ln = La, Pr, Sm, Gd) compounds, Inorg. Mater. 51 (12) (2015) 1213-1218.
8. Dajiang Mei, Shiyan Zhang, Fei Liang, Sangen Zhao, Jianqiao Jiang, Junbo Zhong, Zheshuai Lin, Yuandong Wu, LiGaGe2S6: A chalcogenide with good infrared nonlinear optical performance and low melting point, Inorg. Chem. 56 (21) (2017) 13267-13273.
9. A.A. Ionin, D.V. Badikov, V.V. Badikov, I.O. Kinyaevskiy, Yu.M. Klimachev, A.A. Kotkov, A.Yu. Kozlov, A.M. Sagitova, D.V. Sinitsyn, Sum frequency generation of multi-line slab eadio frequency discharge carbon monoxide laser system with intracavity nonlinear BaGa2GeSe6 crystal, Opt Lett. 43 (18) (2018) 4358-4361.
10. A.O. Fedorchuk, O.V. Parasyuk, O. Cherniushok, B. Andriyevsky, G.L. Myronchuk, O.Y. Khyzhun, G. Lakshminarayana, J. Jedryka, I.V. Kityk, A.M. ElNaggar, A.A. Albassam, M. Piasecki, PbGa2GeS6 crystal as a novel nonlinear optical material: Band structure aspects, J. Alloys Compd. 740 (2018) 294-304.
11. Wan-Jian Yin, Yelong Wu, Su-Huai Wei, Rommel Noufi, Mowafak M. Al-Jassim, Yanfa Yan, Engineering grain boundaries in Cu2ZnSnSe4 for better cell performance: A first-principle study, Adv. Energy Mater. 4 (2014) 1-5.
12. Vishnu Awasthi, Sushil K. Pandey, Saurabh K. Pandey, Shruti Verma, Mukul Gupta, Shaibal Mukherjee, Growth and characterizations of dual ion beam sputtered CIGS thin films for photovoltaic applications, J. Mater. Sci.: Mater. Electron. 25 (7) (2014) 3069–3076.
13. Mai Nguyen, Kaia Ernits, Kong Fai Tai, Chin Fan Ng, Stevin Snellius Pramana, Wardhana A. Sasangka, Sudip K. Batabyal, Timo Holopainen, Dieter Meissner, Axel Neisser, Lydia H.Wong, ZnS buffer layer for Cu2ZnSn(SSe)4 monograin layer solar cell, Solar Energy 111 (2015) 344-349.

14. Kee-Jeong Yang, Dae-Ho Son, Shi-Joon Sung, Jun-Hyoung Sim, Young-Ill Kim, Si-Nae Park, Dong-Hwan Jeon, JungSik Kim, Dae-Kue Hwang, Chan-Wook Jeon, Dahyun Nam, Hyeonsik Cheong, Jin-Kyu Kang, Dae-Hwan Kim, A band-gap-graded CZTSSe solar cell with 12.3% efficiency, J. Mater. Chem. A 4 (2016) 10151-10158.
15. Brajendra S. Sengara, Vivek Garg, Amitesh Kumar, Vishnu Awasthi, Shailendra Kumar, Victor V. Atuchin, Shaibal Mukherjee, Band alignment of Cd-free (Zn, Mg)O layer with Cu2ZnSn(S,Se)4 and its effect on the photovoltaic properties, Opt. Mater. 84 (2018) 748-756.
16. Vivek Garg, Brajendra S. Sengar, Vishnu Awasthi, Amitesh Kumar, Rohit Singh, Shailendra Kumar, C. Mukherjee, V. V. Atuchin, and Shaibal Mukherjee, Investigation of dual-ion beam sputter-instigated plasmon generation in TCOs: A case study of GZO, ACS Appl. Mater. Interfaces 10 (2018) 5464−5474.
17. Amy E. Christuk, Ping Wu, James A. Ibers, New quaternary chalcogenides BaLnMQ3 (Ln = rare earth; M = Cu, Ag; Q = S, Se. I. Structures and grinding-induced phase transition in BaLaCuQ3, J. Solid State Chem. 110 (1994) 330-336.
18. Ping Wu, Amy E. Christuk, James A. Ibers, New quaternary chalcogenides BaLnMQ3 (Ln = rare earth or Sc; M = Cu, Ag; Q = S, Se. II. Structures and property variation vs rare-earth element, J. Solid State Chem. 110 (1994) 337-344.
19. Yuting Yang, James A. Ibers, Synthesis and characterization of a series of quaternary chalcogenides BaLnMQ3 (Ln = rare earth, M = coinage metal, Q = Se or Te), J. Solid State Chem. 147 (1999) 366-371.
20. Fu Qiang Huang, Kwasi Mitchell, James A. Ibers, New layered materials: syntheses, structures, and optical and magnetic properties of CsGdZnSe3, CsZrCuSe3, CsUCuSe3, and BaGdCuSe3, Inorg. Chem. 40 (2001) 5123-5126.
21. Kwasi Mitchell, Fu Qiang Huang, Adam D. McFarland, Christy L. Haynes, Rebecca C. Somers, Richard P. Van Duyne, and James A. Ibers, The CsLnMSe3 Semiconductors (Ln) Rare-Earth Element, Y; M) Zn, Cd, Hg), Inorg. Chem. 42 (2003) 4109-4116.

22. N.V. Sikerina, A.V. Solov'eva, E.N. Toroshchin, O.V. Andreev, Phase equilibria in the BaS-Cu2S-Gd2S3 system, Russ. J. Inorg. Chem. 52 (12) (2007) 1982-1986.
23. N.V. Sikerina, O.V. Andreev, I.P. Leven, Interactions in the SrS-Cu2S-Ln2S3 (Ln = Gd or Er) systems and phase-formation laws in the SrS-Cu2S-Ln2S3 (Ln = La-Lu) systems, Russ. J. Inorg. Chem. 53 (3) (2008) 455-459.
24. A.V. Ruseikina, L.A. Solov'ev, O.V. Andreev, Crystal structures and properties of SrLnCuS3 (Ln = La, Pr) Russ. J. Inorg. Chem. 59 (3) (2014) 196-201.
25. Anna V. Ruseikina, Oleg V. Andreev, Eugenia O. Galenko, Semyon I. Koltsov, Trends in thermodynamic parameters of phase transitions of lanthanide sulfides SrLnCuS3 (Ln = La-Lu), J. Therm. Anal. Calorim. 128 (2) (2017) 993-999.
26. A.V. Ruseikina, O.V. Andreev, Regularities of change in the structural parameters of EuLnCuS3 (Ln = La-Nd, Sm, Gd, Ho), Russ. J. Inorg. Chem. 62 (2) (2017) 160-167.
27. A.V. Ruseikina, S.I. Kol'tsov, O.V. Andreev, L.A. Pimneva, Crystal structure of EuLnAgS3 (Ln = Gd and Ho) compounds, Russ. J. Inorg. Chem. 62 (12) (2017) 1632-1637.
28. A.V. Ruseikina, O.V. Andreev, Phase equilibria in systems DyCuS2-Eu-S and Cu2S-Dy2S3-EuS, Russ. J. Inorg. Chem. 63 (11) (2018) 1494-1500.
29. P. Lemoine, D. Carre, M. Guittard, Structure du sulfure d'europium et de cuivre Eu2CuS3, Acta Cryst. C42 (1986) 390-391.
30. M.F. Mansuetto, P.M. Keane, J.A. Ibers, Synthesis, structure, and conductivity of the new group IV chalcogenides KCuZrQ3 (Q = S, Se, Te), J. Solid State Chem. 101 (1992) 257-264.
31. N.A. Khritohin, O.V. Andreev, O.V. Mitroshin, A.S. Korotkov, Thermodynamics of phase changes in systems BaS-Ln2S3 (Ln = Pr, Sm, Gd, Tb, Er, Lu, J. Phase Equilib. Diffusion 25 (6) (2004 515-519.
32. A.V. Ruseikina, O.V. Andreev, Phase equilibria in the Cu2S-La2S3-EuS system, Russ. J. Inorg. Chem. 62 (5) (2017) 610-618.

33. Michihiro Ohta, Shinji Hirai, Hisanaga Kato, Vladimir V. Sokolov, Vladimir V. Bakovets.: Thermal Decomposition of NH4SCN for Preparation of Ln2S3 (Ln=La and Gd) by Sulfurization. Mater. Trans. 50 (7) (2009) 1885-1889.
34. NETZSCH Proteus 6. Thermic analyses – User's and software manuals, Germany. 2012.
35. Bruker AXS TOPAS V4: General profile and structure analysis software for powder diffraction data. – User's Manual. Bruker AXS, Karlsruhe, Germany. 2008.
36. Hugh D. Selby, Benny C. Chan, Ryan F. Hess, Kent D. Abney, Peter K. Dorhout, Three new phases in the K/Cu/Th/S system: $KCuThS_3$, $K_2Cu_2ThS_4$, and $K_3Cu_3Th_2S_7$, Inorg. Chem. 44 (18) (2005) 6463-6469.
37. J. Huster, W. Bronger, α--und β-BaCu2X2 (X ≙ S, Se) – Darstellung von Einkristallen in Kaliumchalkogenocyanat-Schmelzen, Z. Anorg. Allgem. Chem. 625 (12) (1999) 2033-2040.
38. https://www.python.org/
39. A.V. Ruseikina, L.A. Solovyev, O.V. Andreev, A.A. Kislitsyn, $EuNdCuS_3$: crystal structure of the high-temperature polymorph and properties, Russ. J. Inorg. Chem. 59 (10) (2014) 1109-1114.
40. Marcel A. Eberle, Sabine Strobel, Thomas Schleid, $SrCuNdS_3$: a new compound with two different crystal structures. Jahrestagung der DGK, Berlin, 17-20 Maerz 2014' 2014 1 MS05-48, MS05-48 DUMMY7.
41. I. Kohatsu, B.J. Wuensch, The crystal structure of aikinite, PbCuBiS3, Acta Cryst. B 27 (6) (1971) 1245-1252.
42. S. Strobel, T. Schleid, Three structure types for strontium copper (I) lanthanide (III) selenides SrCuMSe3 (M= La, Gd, Lu), J. Alloys Compd. 418 (1-2) (2006) 80-85.
43. A.V. Ruseikina, L.A. Solov'ev, O.V. Andreev, Crystal structures of α-and β-EuPrCuS3, Russ. J. Inorg. Chem. 58 (10) (2013) 1231-1236.
44. N.V. Sikerina, O.V. Andreev, Crystal structures of SrLnCuS 3 (Ln= Gd, Lu), Russ. J. Inorg. Chem. 52 (4) (2007) 581-584.

45. S. Strobel, T. Schleid, Quaternäre Strontium-Kupfer (I)-Lanthanoid (III)-Selenide mit Cer und Praseodym: SrCuCeSe3 und SrCuPrSe3, ein ungleiches Geschwisterpaar/Quaternary Strontium Copper (I) Lanthanoid (III) Selenides with Cerium and Praseodymium: SrCuCeSe3 and SrCuPrSe3, Unequal Brother and Sister. Z. Naturforsch. B 59 (9) (2004) 985-991.
46. A.V. Ruseikina, L.A. Solov'ev, Crystal Structures of α-and β-SrCeCuS3, Russ. J. Inorg. Chem. 61 (4) (2016) 482-487.
47. A.V. Ruseikina, L.A. Solovyov, M.S. Molokeev, O.V. Andreev, Crystal structures of EuLnCuS 3 (Ln= Nd and Sm), Russ. J. Inorg. Chem. 57 (1) (2012) 79-83.
48. F. Furuuchi, M. Wakeshima, Y. Hinatsu, Magnetic properties and ^{151}Eu Mössbauer effects of mixed valence europium copper sulfide, Eu2CuS3. J. Solid State Chem. 177 (11) (2004) 3853-3858.
49. L.D. Gulay, I.D. Olekseyuk, Crystal structures of the RCuPbSe3 (R= Gd, Tb, Dy, Ho, Er, Tm, Yb and Lu) compounds, J. Alloys Compd. 387 (1-2) (2005) 160-164.
50. M. Wakeshima, F. Furuuchi, Y. Hinatsu, Crystal structures and magnetic properties of novel rare-earth copper sulfides, EuRCuS3 (R= Y, Gd–Lu), J. Phys.: Condens. Matter 16 (30) (2004) 5503.
51. L.D. Gulay, M.R. Huch, I.D. Olekseyuk, J. Stępień-Damm, A. Pietraszko, Crystal structures of the compounds Yb5.5AgSe8, YbAgSe2 and YxYb1−xCuYbSe3 (x= 0.11), J. Alloys Compd. 428 (1-2) (2007) 139-145.
52. S. Maier, J. Prakash, D. Berthebaud, O. Perez, S. Bobev, F. Gascoin, Crystal structures of the four new quaternary copper (I)-selenides A0.5CuZrSe3 and ACuYSe3 (A= Sr, Ba), J. Solid State Chem. 242 (2016) 14-20.
53. L.D. Gulay, V.Y. Shemet, I.D. Olekseyuk, Crystal structures of the compounds YCuS2, Y3CuSnS7 and YCuPbS3, J. Alloys Compd. 388 (1) (2005) 59-64.

54. F.Q. Huang, J.A. Ibers, New layered materials: Syntheses, structures, and optical properties of K2TiCu2S4, Rb2TiCu2S4, Rb2TiAg2S4, Cs2TiAg2S4, and Cs2TiCu2Se4, Inorg. Chem. 40 (11) (2001) 2602-2607.
55. Anna V. Ruseykina, Alexander V. Kertman, Synthesis of compounds EuLnCuS3 (Ln=La-Nd), temperature and enthalpy of melting, Vestnik of the Tumen State University, 3 (2010) 221-227 (in Russian).
56. Petr O. Andreev, Aleksei A. Polkovnikov, Yuriy G. Denisenko, Oleg V. Andreev, Tatyana M. Burkhanova, Andrey N. Bobylev, Ludmila A. Pimneva, Temperatures and enthalpies of melting of Ln2S3 (Ln = Gd, Tb, Dy, Ho, Er, Tm, Yb, and Lu) compounds, J. Therm. Anal. Calorim. 131 (2) (2018) 1545–1551.
57. Adel Mesbah, Sébastien Lebègue, Jordan M. Klingsporn, Wojciech Stojko, Richard P. Van Duyne, James A. Ibers, Synthesis, crystal structure, and optical properties of Ba2Cu2ThS5, and electronic structures of Ba2Cu2ThS5 and Ba2Cu2US5, J. Solid State Chem. 200 (2013) 349-353.
58. Anna V. Ruseikina, Leonid A. Solovyov, Vladimir A. Chernyshev, Aleksandr S. Aleksandrovsky, Oleg V. Andreev, Svetlana N. Krylova, Alexander S. Krylov, Dmitriy A. Velikanov, Maxim S. Molokeev, Nikolai G. Maximov, Maxim V. Grigoriev, Alexander A. Garmonov, Alexey V. Matigorov. Synthesis, Structure, and Properties of EuErCuS3. J. Alloys and Compounds. 805. (2019) 779 - 788.
59. E. Kroumova, M.I. Aroyo, J.M. Perez-Mato, A. Kirov, C. Capillas, S. Ivantchev, H. Wondraschek, Bilbao Crystallographic Server : Useful databases and tools for phase-transition studies, Phase Transit. 76 (2003), 155-170.
60. M.B. Smirnov, V.Yu. Kazimirov, LADY: software for lattice dynamics simulations. (JINR communications), E 14-2001-159, 2001.
61. M. Smirnov, R. Baddour-Hadjean, Li intercalation in TiO_2 anatase: Raman spectroscopy and lattice dynamic studies, J. Chem. Phys. 121 (2004) 2348-2355.

62. Yu.G. Denisenko, V.V. Atuchin, M.S. Molokeev, A.S. Aleksandrovsky, A.S. Krylov, A.S. Oreshonkov, S.S. Volkova, O.V. Andreev, Structure, Thermal Stability, and Spectroscopic Properties of Triclinic Double Sulfate AgEu(SO4)2 with Isolated SO4 Groups, Inorganic Chemistry. 57 (2018) 13279-13288.
63. V.V. Atuchin, A.S. Aleksandrovsky, M.S. Molokeev, A.S. Krylov, A.S. Oreshonkov, D. Zhou, Structural and spectroscopic properties of self-activated monoclinic molybdate $BaSm_2(MoO_4)_4$, J. Alloy. Compd. 729 (2017) 843–849.
64. Chang Sung Lim, Aleksandr S. Aleksandrovsky, Maxim S. Molokeev, Aleksandr S. Oreshonkov, Victor V. Atuchin, Microwave synthesis and spectroscopic properties of ternary scheelite-type molybdate phosphors $NaSrLa(MO_4)_3:Er^{3+}/Yb^{3+}$, J. Alloys Compd. 713 (2017) 156-163.
65. C.S. Lim, A.S. Aleksandrovsky, M.S. Molokeev, A.S. Oreshonkov, D.A. Ikonnikov and V.V. Atuchin, Triple molybdate scheelite-type upconversion phosphor $NaCaLa(MoO_4)_3:Er^{3+}/Yb^{3+}$: structural and spectroscopic properties, Dalton Trans. 45 (2016) 15541-15551.
66. A.S. Oreshonkov, J.V. Gerasimova, A.A. Ershov, A.S. Krylov, K.A. Shaykhutdinov, A.N. Vtyrin, M.S. Molokeev, K.Y. Terent'ev and N.V. Mihashenok, Raman spectra and phase composition of $MnGeO_3$ crystals, J. Raman Spectr. 47 (2016) 531–536.
67. V.V. Atuchin, A.S. Aleksandrovsky, O.D. Chimitova, T.A. Gavrilova, A.S. Krylov, M.S. Molokeev, A.S. Oreshonkov, B.G. Bazarov, J.G. Bazarova, Synthesis and spectroscopic properties of monoclinic α-$Eu_2(MoO_4)_3$, J. Phys. Chem. C 118 (2014) 15404-15411.
68. Zhiguo Xia, M.S. Molokeev, A.S. Oreshonkov, V.V. Atuchin, Ru-Shi Liu, Cheng Dong, Crystal and local structure refinement in $Ca_2Al_3O_6F$ explored by X-ray diffraction and Raman spectroscopy, Phys. Chem. Chem. Phys. 16 (2014) 5952-5957.

Table 1. Main parameters of processing and refinement of the $BaPrCuS_3$ and BaSmCuS3 samples

Compound	$BaPrCuS_3$	$BaSmCuS_3$
Sp. Gr.	*Pnma*	*Cmcm*
a, Å	10.56074 (6)	4.07269 (4)
b, Å	4.11305 (2)	13.4499 (1)
c, Å	13.42845 (7)	10.3704 (1)
V, Å^3	583.289 (5)	568.06 (1)
Z	2	2
2θ-interval, º	10-150	10-150
R_{wp}, %	1.18	1.84
R_p, %	1.20	1.39
R_{exp}, %	0.62	0.86
χ^2	1.89	2.14
R_B, %	0.79	0.88

Table 2. Fractional atomic coordinates and isotropic or equivalent isotropic displacement parameters (Å^2) of $BaPrCuS_3$ and $BaSmCuS_3$

	x	*y*	*z*	U_{iso}*/U_{eq}
		$BaPrCuS_3$		
Pr	0.00804 (8)	0.25	0.75733 (6)	0.0041 (4)
Cu	0.2406 (2)	0.25	0.28297 (9)	0.0093 (4)*
Ba	0.26735 (8)	0.25	0.00560 (4)	0.0178 (5)
S1	0.0555 (2)	0.25	0.3822 (2)	0.0038 (6)*
S2	0.2558 (3)	0.25	0.6825 (1)	0.0039 (5)*
S3	0.4181 (2)	0.25	0.3905 (2)	0.0070 (7)*
		$BaSmCuS_3$		
Sm	0.5	0	0	0.71 (3)
Cu	0.5	0.53447 (15)	0.25	1.01 (6)*
Ba	0.5	0.25634 (7)	0.25	1.07 (12)
S1	0.5	0.63449 (19)	0.0670 (2)	0.85 (7)*
S2	0.5	0.9328 (2)	0.25	1.10 (10)*

Table 3. Temperature of melting and enthalpy of melting in compounds $ABCuS_3$

Compound	T_{melt}, K	H_{melt}, kJ·mol^{-1}	Reference
$SrLaCuS_3$	1513	6,9	24,25
$SrCeCuS_3$	1468	5,2	25,46
$SrPrCuS_3$	1459	13,2	25
$SrNdCuS_3$	1429	16,8	25
$SrSmCuS_3$	1605	2,8	25
$EuLaCuS_3$	1539	23,4	32, 55
$EuCeCuS_3$	1524	23,7	55
$EuPrCuS_3$	1497	20,1	55
$EuNdCuS_3$	1470	17,7	39,55
$EuDyCuS_3$	1727	2,9	28
$BaGdCuS_3$	1685	-	39
$BaPrCuS_3$	1580.9	86.6	This study

Captions

Figure 1. Photo of (a) $BaPrCuS_3$ and (b) $BaSmCuS_3$ samples.

Figure 2. Difference Rietveld plots of (a) $BaPrCuS_3$ and (b) $BaSmCuS_3$.

Figure 3. Crystal structures of (a) $BaPrCuS_3$ and (b) $BaSmCuS_3$ sulfides. The anisotropic thermal parameters of Pr^{3+}, Sm^{3+} and Ba^{2+} ions are shown at the 50% probability level.

Figure 4. Structure types in known $ABCX_3$ (X = S, Se) crystals.

Figure 5. SEM image of $BaPrCuS_3$ powder.

Figure 6. DTA curves recorded for $BaPrCuS_3$. The baselines are shown in red color.

Figure 7. Tauc plot for $BaPrCuS_3$.

Figure 8. Raman spectra of $BaPrCuS_3$ and $BaSmCuS_3$. The black, red, blue and green vertical ticks mark the calculated wavenumbers of Raman-active vibrational modes.

Figure 9. Examples of calculated vibrational modes in $BaPrCuS_3$, (a) A_g 20.6 cm^{-1} low frequency layer vibration, (e) A_g 202.5 cm^{-1} related to the vibration of bridging oxygen atoms and, in $BaSmCuS_3$, (b) and (c) A_g 64.6 cm^{-1} and B_{3g} 68.6 cm-1 layer vibrations, respectively, (d) A_g 209.2 cm^{-1} O-S–O bending-like vibration, (f) A_g 330.6 cm^{-1} S-O stretching-like vibration.

a

b

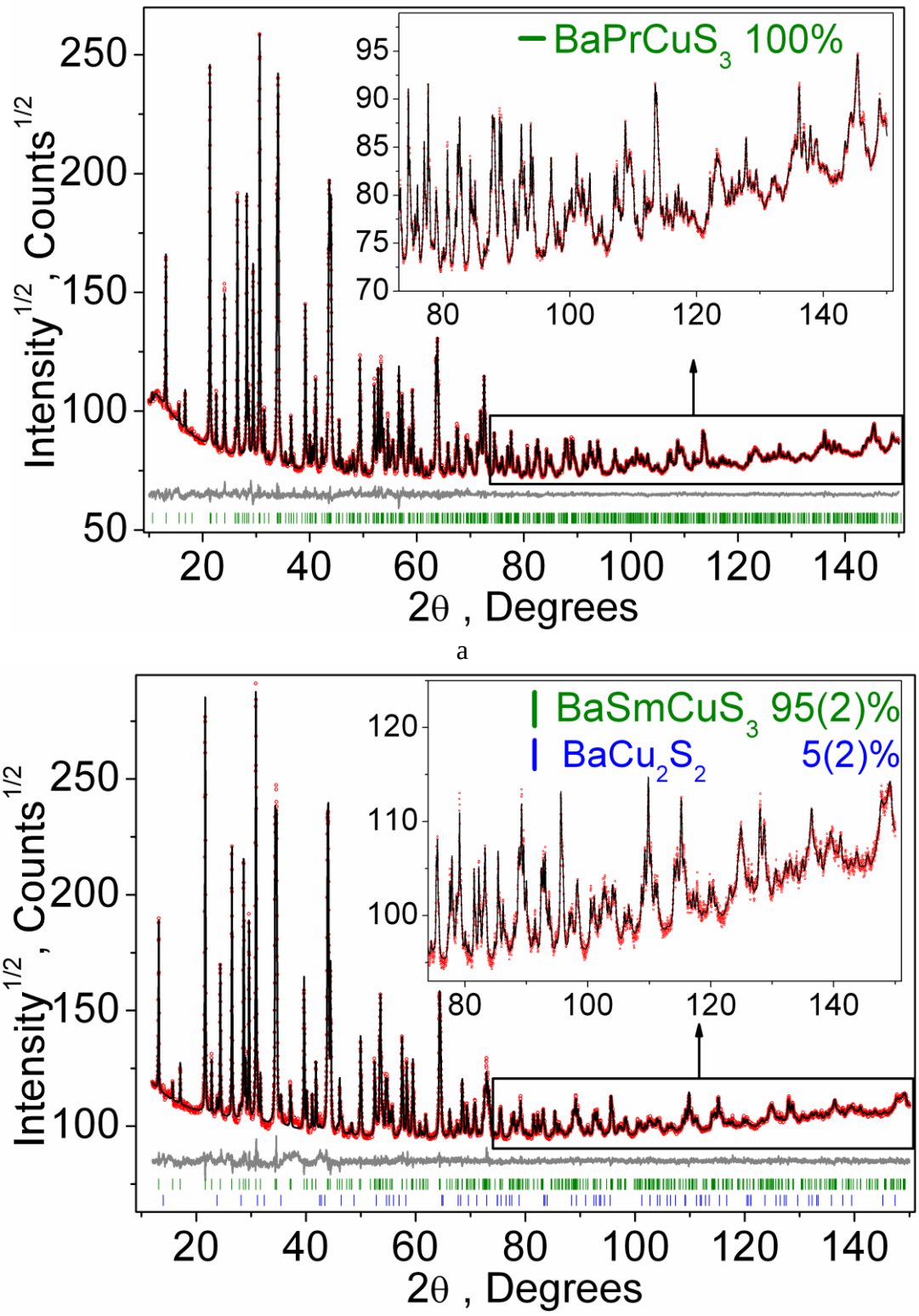
BaPrCuS3 100%
Intensity1/2, Counts1/2
2θ , Degrees
a
BaSmCuS3 95(2)%
BaCu2S2 5(2)%
Intensity1/2, Counts1/2
2θ , Degrees
b

Figure 2

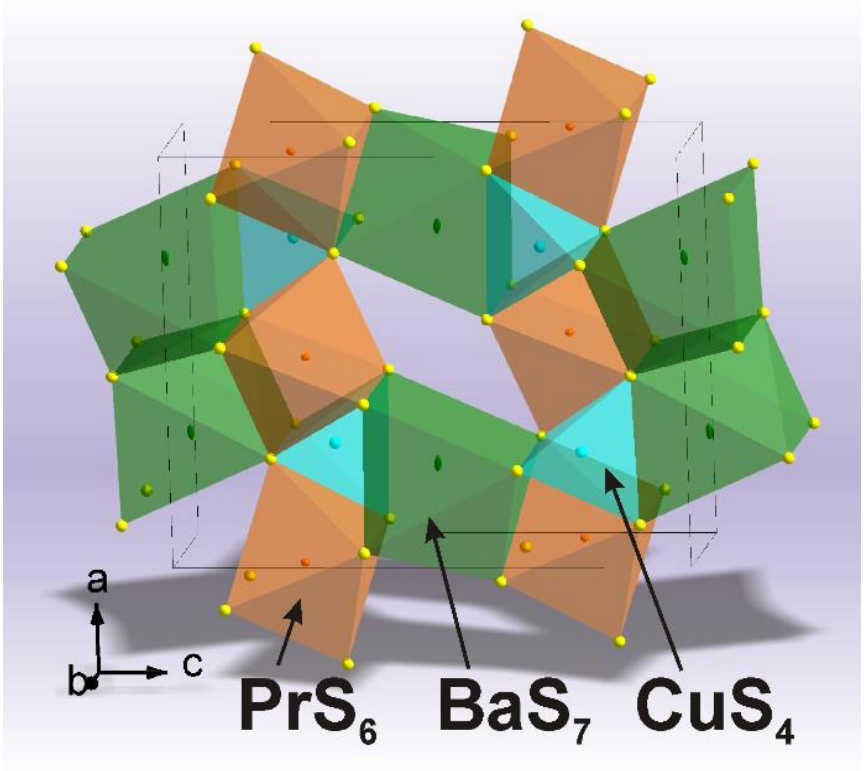

a

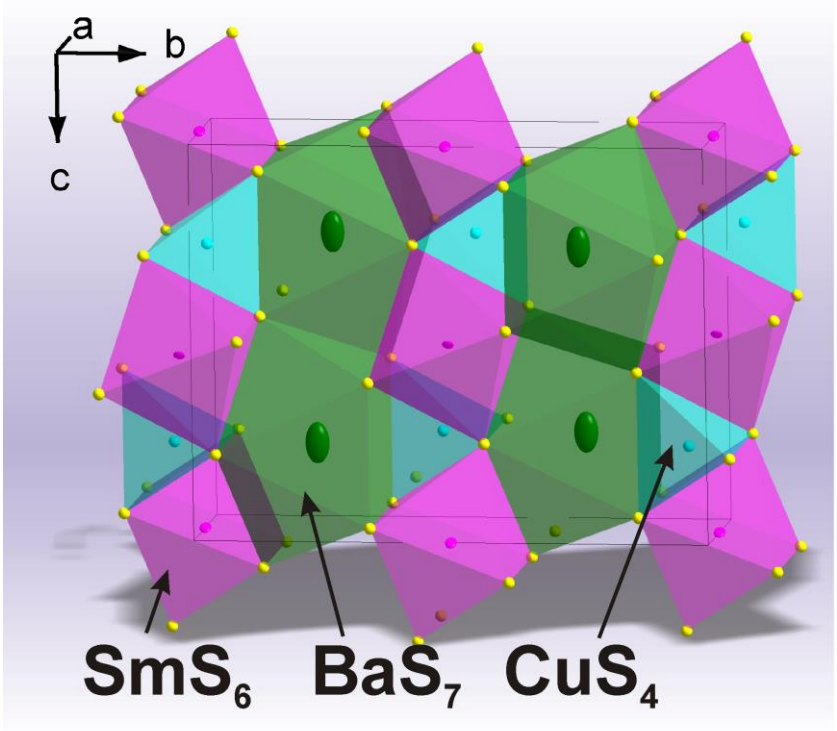

b

Figure 3

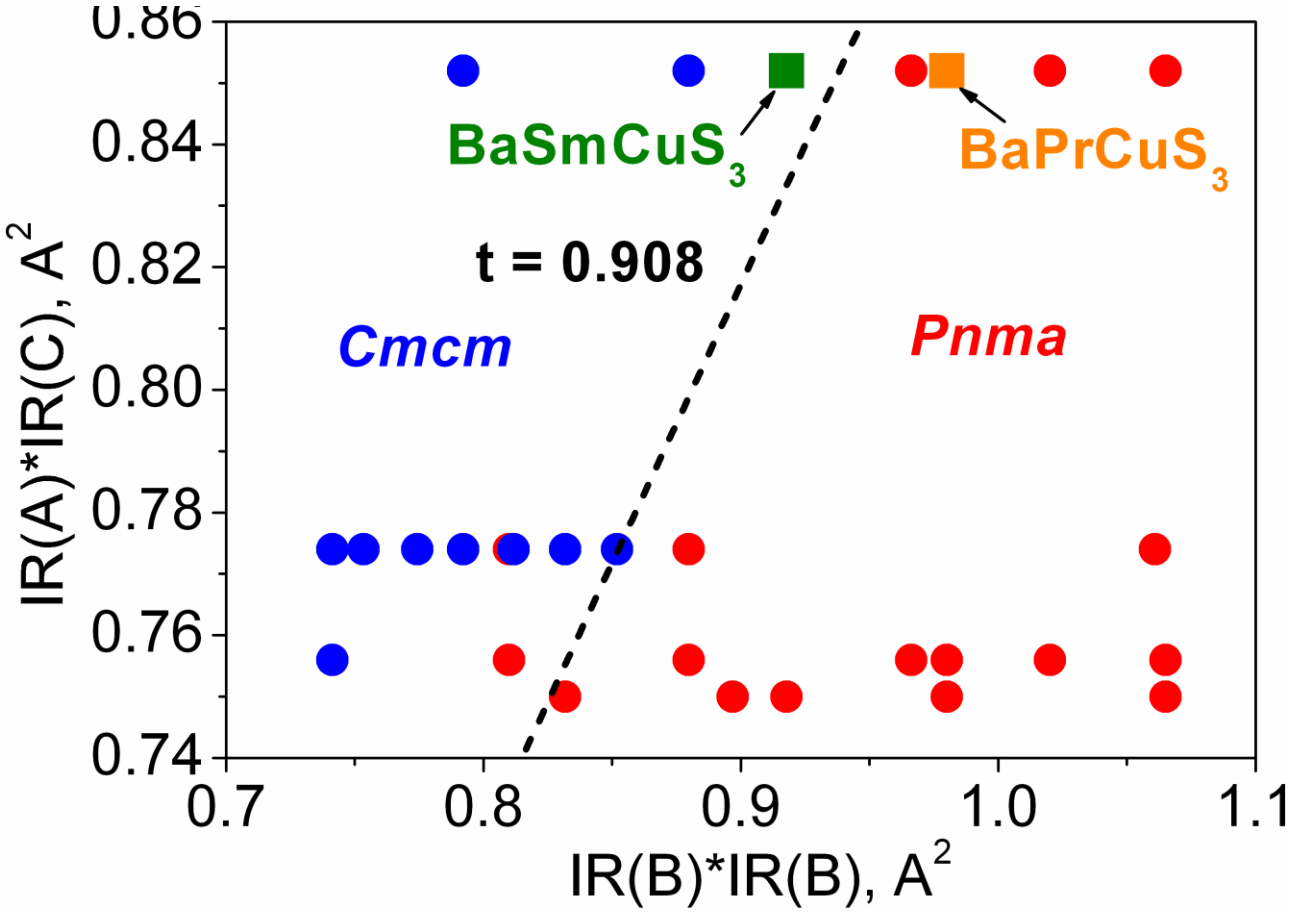
0.86
0.84
0.82
0.80
0.78
0.76
0.74
IR(A)*IR(C), A2
0.7
0.8
0.9
1.0
1.1
IR(B)*IR(B), A2
BaSmCuS3
BaPrCuS3
t = 0.908
Cmcm
Pnma

Figure 4

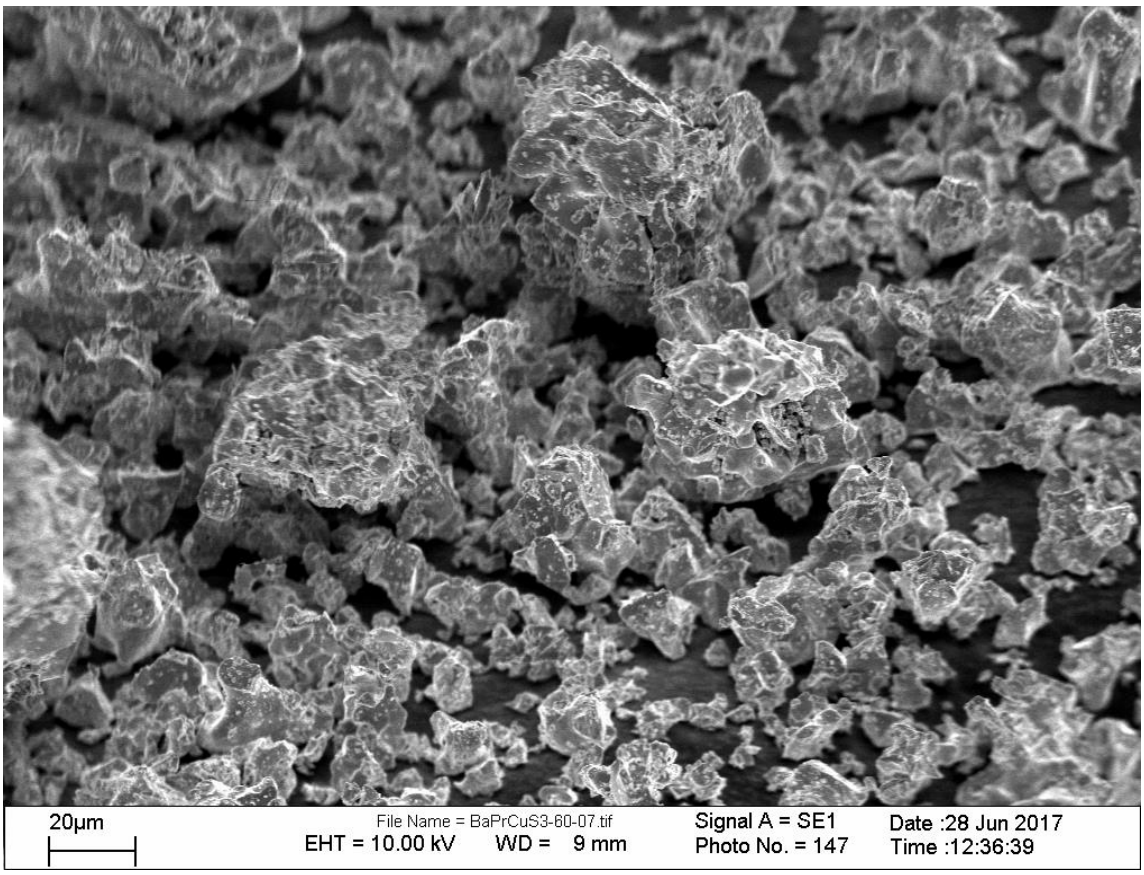
20µm
File Name = BaPrCuS3-60-07.tif
EHT = 10.00 kV
WD = 9 mm
Signal A = SE1
Photo No. = 147
Date :28 Jun 2017
Time :12:36:39

Figure 5

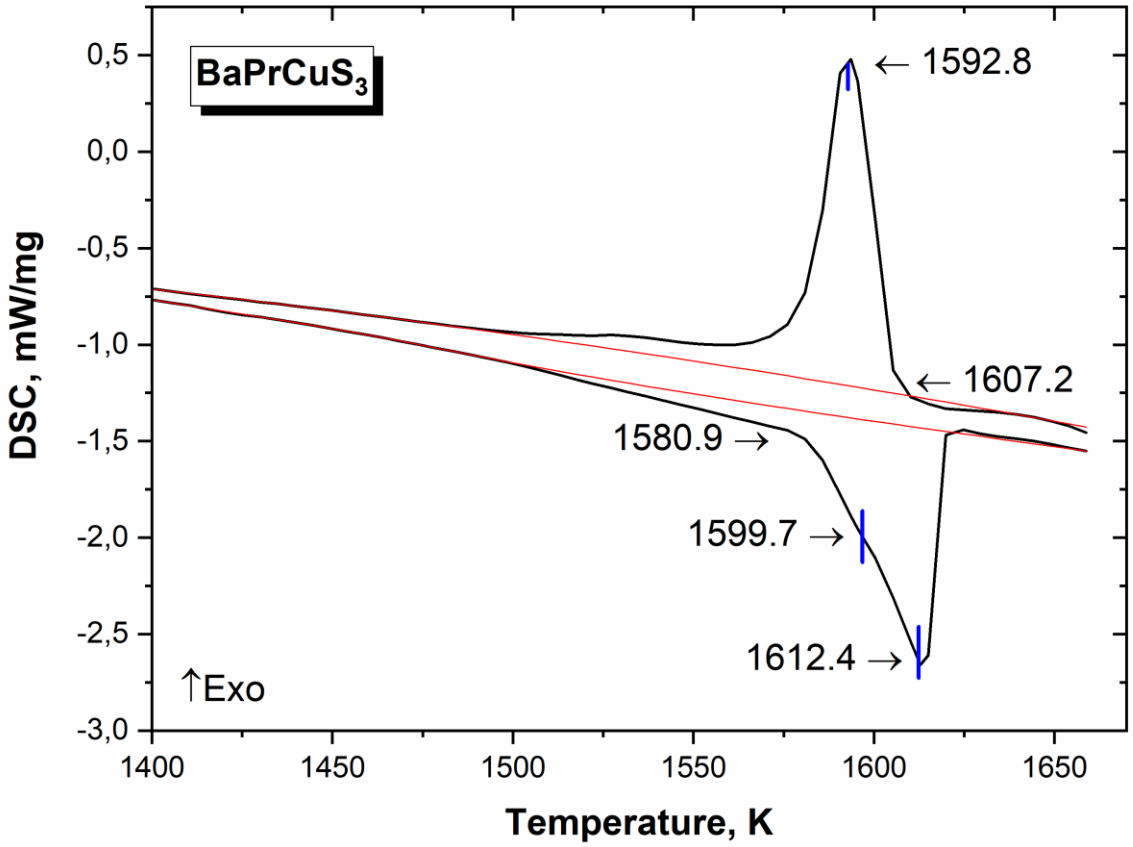
BaPrCuS3
← 1592.8
← 1607.2
1580.9 →
1599.7 →
1612.4 →
↑Exo
DSC, mW/mg
Temperature, K
0,5
0,0
-0,5
-1,0
-1,5
-2,0
-2,5
-3,0
1400
1450
1500
1550
1600
1650

Figure 6.

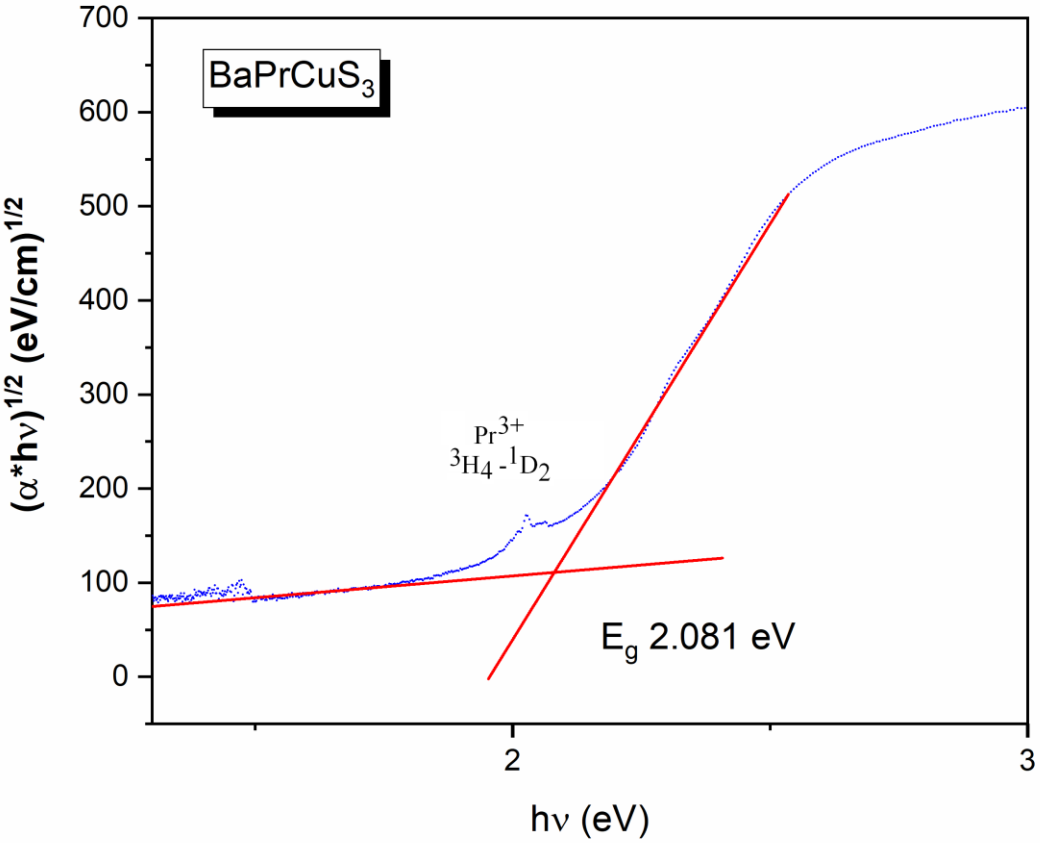
BaPrCuS3
700
600
500
400
300
200
100
0
(α*hν)1/2 (eV/cm)1/2
Pr3+
3H4 - 1D2
Eg 2.081 eV
2
3
hν (eV)

Figure 7

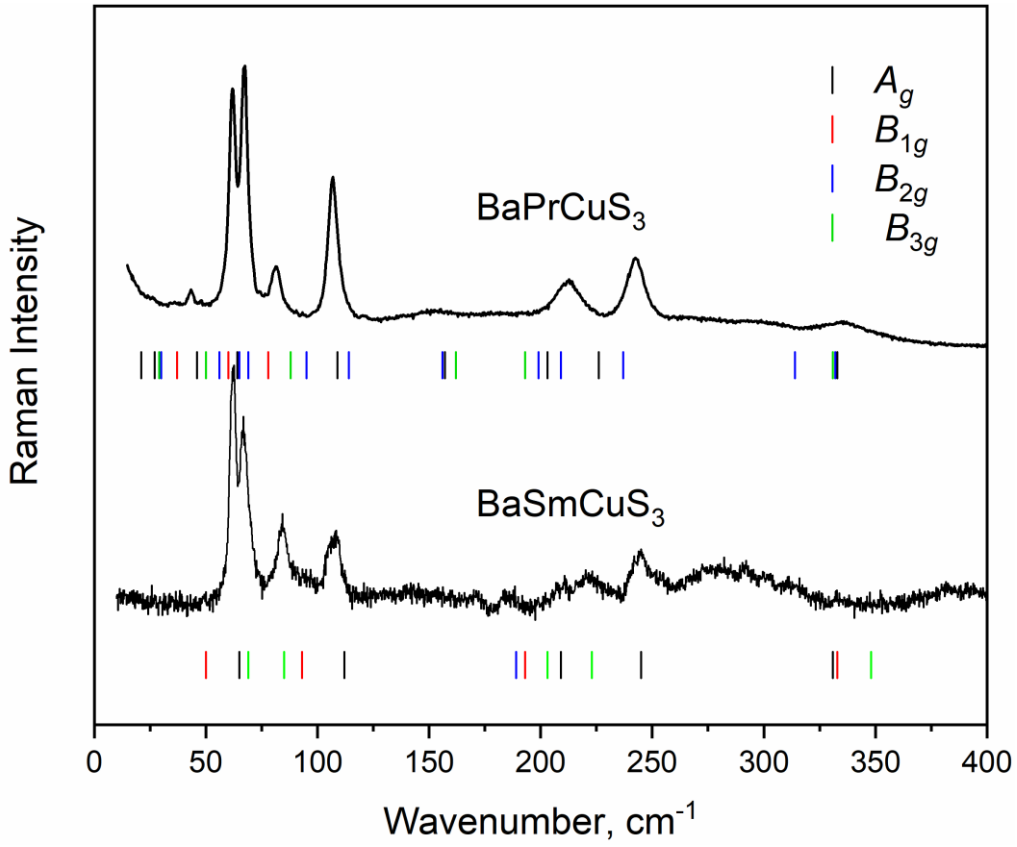
Raman Intensity
BaPrCuS3
BaSmCuS3
Ag
B1g
B2g
B3g
0
50
100
150
200
250
300
350
400
Wavenumber, cm-1

Figure 8

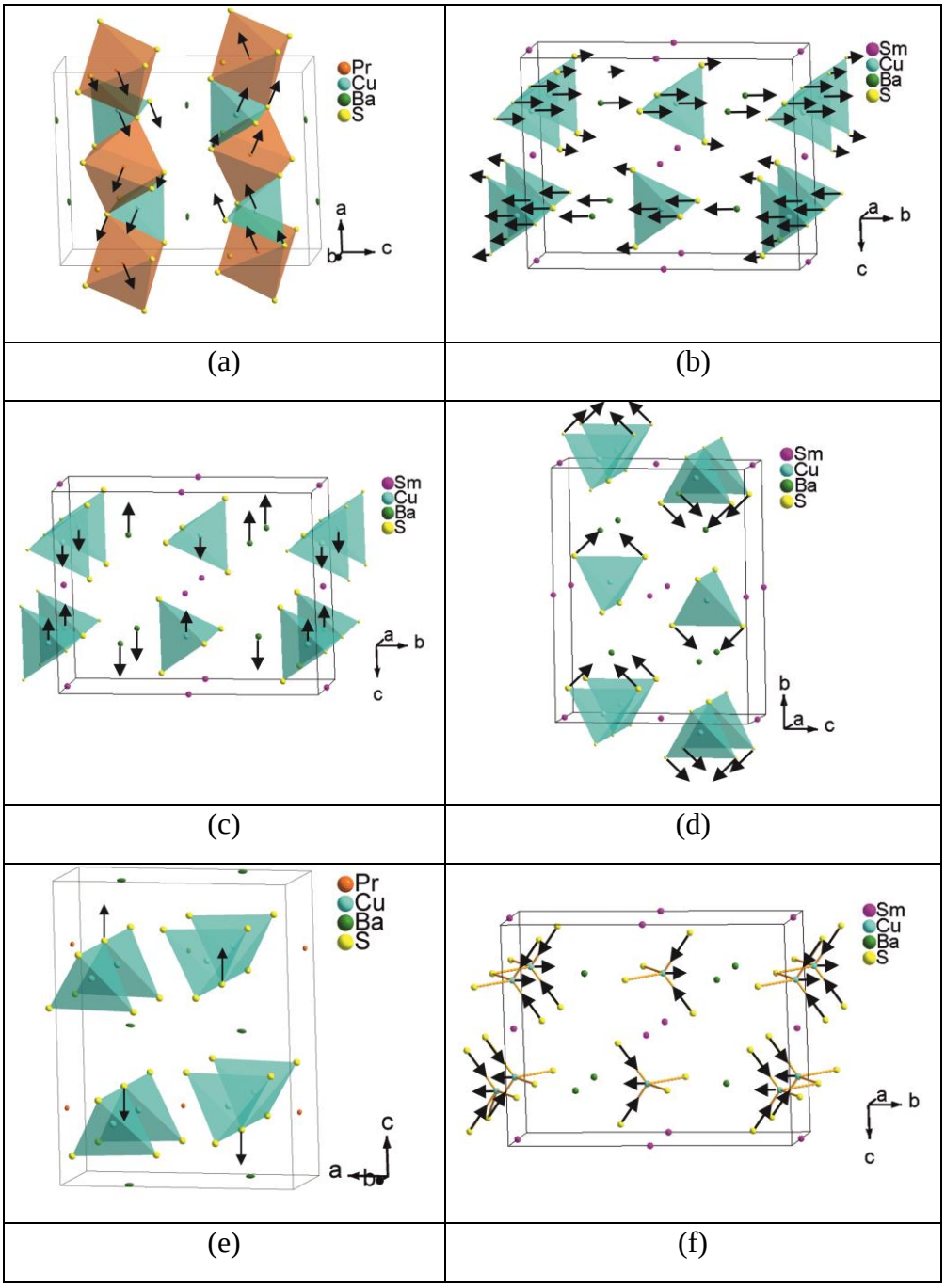
Pr
Cu
Ba
S
a
b
c
Sm
Cu
Ba
S
a
b
c
Sm
Cu
Ba
S
a
b
c
Sm
Cu
Ba
S
b
a
c
Pr
Cu
Ba
S
c
a
b
Sm
Cu
Ba
S
a
b
c

(a) (b)

(c) (d)

(e) (f)

Fig. 9

Supporting information

Synthesis, structural and spectroscopic properties of orthorhombic compounds BaLnCuS3 (Ln = Pr, Sm)

Nikita O. Azarapin1, Aleksandr S. Aleksandrovsky2,3, Victor V. Atuchin4,5,6, Tatyana A. Gavrilova7, Aleksandr S. Krylov8, Maxim S. Molokeev9,10,11, Shaibal Mukherjee12, Aleksandr S. Oreshonkov8,11, Oleg V. Andreev1

1Institute of Chemistry, Tyumen State University, Tyumen 625003, Russia

2Laboratory of Coherent Optics, Kirensky Institute of Physics Federal Research Center KSC SB RAS, Krasnoyarsk 660036, Russia

3Department of Photonics and Laser Technologies, Siberian Federal University, Krasnoyarsk 660041, Russia

4Laboratory of Optical Materials and Structures, Institute of Semiconductor Physics, SB RAS, Novosibirsk 630090, Russia

5Functional Electronics Laboratory, Tomsk State University, Tomsk 634050, Russia

6Research and Development Department, Kemerovo State University, Kemerovo 650000, Russia

7Laboratory of Nanodiagnostics and Nanolithography, Institute of Semiconductor Physics, SB RAS, Novosibirsk 630090, Russia

8Laboratory of Molecular Spectroscopy, Kirensky Institute of Physics Federal Research Center KSC SB RAS, Krasnoyarsk 660036, Russia

9Laboratory of Crystal Physics, Kirensky Institute of Physics Federal Research Center KSC SB RAS, Krasnoyarsk 660036, Russia

10Department of Physics, Far Eastern State Transport University, Khabarovsk 680021, Russia

11Siberian Federal University, Krasnoyarsk 660079, Russia

12Hybrid Nanodevice Research Group (HNRG), Electrical Engineering, Indian Institute of Technology Indore, Madhya Pradesh 453552, India

Table 1S. Main bond lengths (Å) of $BaPrCuS_3$ and $BaSmCuS_3$

$BaPrCuS_3$			
Pr—S1^{i}	2.862 (2)	Cu—S3	2.366 (3)
Pr—S2	2.803 (3)	Ba—S1^{iv}	3.237 (2)
Pr—S2^{ii}	2.784 (3)	Ba—S1^{v}	3.396 (3)
Pr—S3^{iii}	2.835 (2)	Ba—S2^{iv}	3.151 (2)
Cu—S1	2.366 (3)	Ba—S3^{iv}	3.233 (2)
Cu—S2^{iv}	2.460 (1)		
$BaSmCuS_3$			
Sm—S1^{i}	2.8110 (17)	Cu—S2^{iii}	2.453 (2)
Sm—S2^{ii}	2.7457 (11)	Ba—S1^{iii}	3.230 (2)
Cu—S1	2.326 (3)	Ba—S2^{iii}	3.127 (3)

Symmetry codes:

$BaPrCuS_3$: (i) -*x*, -*y*, -*z*+1; (ii) *x*-1/2, -*y*+1/2, -*z*+3/2; (iii) -*x*+1/2, -*y*, *z*+1/2; (iv) -*x*+1/2, -*y*, *z*-1/2; (v) *x*+1/2, -*y*+1/2, -*z*+1/2

$BaSmCuS_3$: (i) -*x*+1/2, -*y*+1/2, -*z*; (ii) *x*, *y*-1, *z*; (iii) -*x*+1/2, *y*-1/2, -*z*+1/2

Table 2S. Atomic displacement parameters (Å^2)

	U^{11}	U^{22}	U^{33}	U^{12}	U^{13}	U^{23}
$BaPrCuS_3$						
Pr	0.0041 (4)	0.0039 (3)	0.0058 (4)	0	-0.0003 (3)	0
Ba	0.0178 (5)	0.0021 (4)	0.0036 (4)	0	-0.0010 (3)	0
$BaSmCuS_3$						
Sm	0.0109 (7)	0.0100 (8)	0.0062 (8)	0	-0.0060 (6)	0
Ba	0.0061 (8)	0.0086 (9)	0.0257 (1)	0	0	0

Table 3S. Chemical formulas, space groups and corresponding tolerance factors of $ABCX_3$ compounds

Compound	t = IR(A)*IR(C)/IR(B)^2	Space group	Reference
$EuNdCuS_3$	0.704209	*Pnma*	[39]
$SrNdCuS_3$	0.709843	*Pnma*	[40]
$PbBiCuS_3$	0.729569	*Pnma*	[41]
$SrLaCuSe_3$	0.741104	*Pnma*	[42]
$SrLaCuS_3$	0.741104	*Pnma*	[24]
$EuPrCuS_3$	0.765228	*Pnma*	[43]
$SrPrCuS_3$	0.77135	*Pnma*	[44]
$SrPrCuSe_3$	0.77135	*Pnma*	[45]
$SrCeCuS_3$	0.782375	*Pnma*	[46]
$SrCeCuSe_3$	0.782375	*Pnma*	[45]
$BaNdCuS_3$	0.799982	*Pnma*	[18]
$EuSmCuS_3$	0.817204	*Pnma*	[47]
$BaLaCuS_3$	0.835212	*Pnma*	[17]
$BaLaCuSe_3$	0.835212	*Pnma*	[17]
Eu_2CuS_3	0.836298	*Pnma*	[48]
$SrGdCuS_3$	0.859243	*Pnma*	[44]
$SrGdCuSe_3$	0.859243	*Pnma*	[42]
$PbGdCuSe_3$	0.879701	*Pnma*	[49]
$BaCeCuS_3$	0.881724	*Pnma*	[18]
$BaCeCuSe_3$	0.881724	*Pnma*	[18]
$EuDyCuS_3$	0.90172	*Pnma*	[50]
$Y_{0.11}Yb_{0.89}YbCuS_3$	0.907855	*Pnma*	[51]
$PbTbCuS_3$	0.908526	*Cmcm*	[49]
$PbDyCuS_3$	0.930575	*Cmcm*	[49]
$SrYCuSe_3$	0.933333	*Pnma*	[52]
$PbHoCuS_3$	0.953436	*Cmcm*	[49]
$PbYCuS_3$	0.955556	*Pnma*	[53]
$BaGdCuS_3$	0.968353	*Cmcm*	[18]
$BaGdCuSe_3$	0.968353	*Cmcm*	[54]
$BaLaCuS_3$	0.977149	*Cmcm*	[17]
$PbTmCuS_3$	0.999483	*Cmcm*	[14]

$SrLuCuS_3$	1.019801	*Cmcm*	[44]
$SrLuCuSe_3$	1.019801	*Cmcm*	[42]
$PbYbCuS_3$	1.02731	*Cmcm*	[14]
$PbLuCuS_3$	1.044082	*Cmcm*	[14]
$BaErCuS_3$	1.075622	*Cmcm*	[18]
$BaErCuSe_3$	1.075622	*Cmcm*	[18]
$BaLaAgSe_3$	1.39202	*Cmcm*	[18]
$BaErAgSe_3$	1.792703	*Cmcm*	[18]
$BaGdAuSe_3$	2.001264	*Cmcm*	[19]

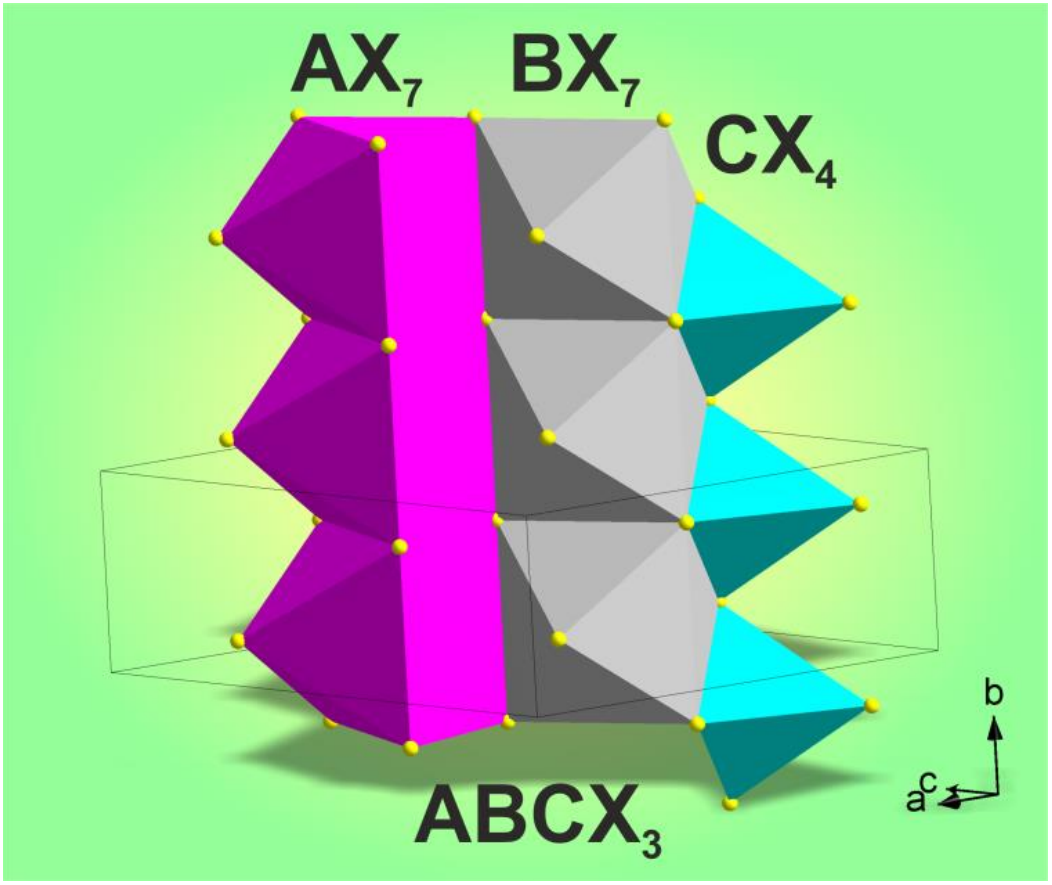

Figure S1. Three columns of polyhedra: AX_7, BX_7 and CX_4 which are linked with each other by edges.

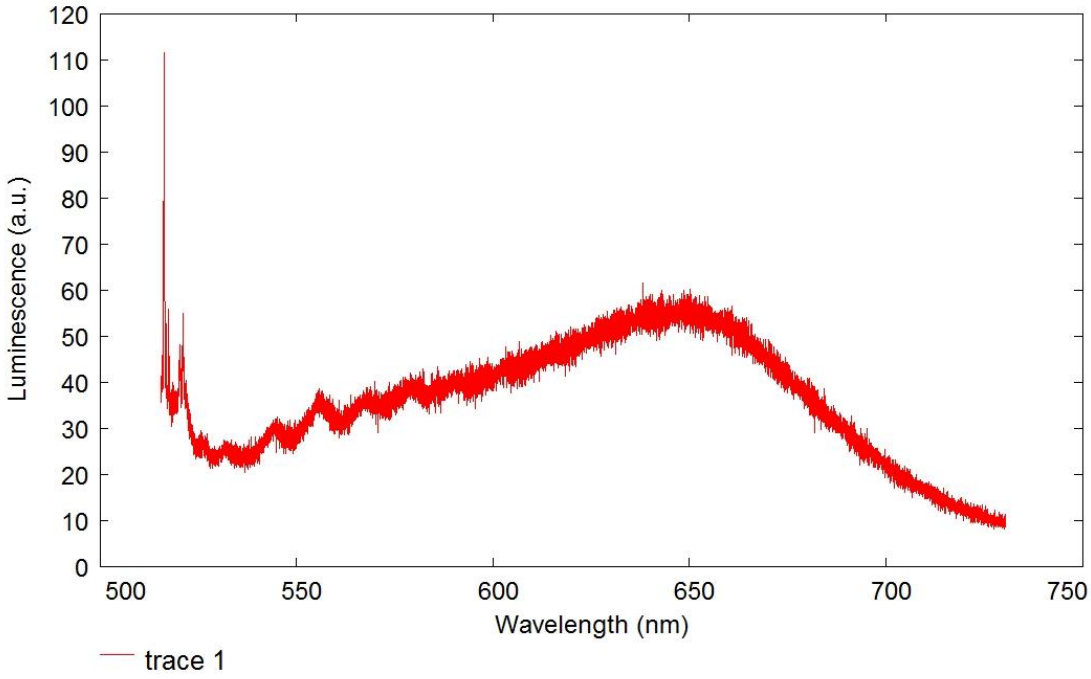

Figure S2. Emission spectrum of $BaPrCuS_3$ recorded under the excitation at 514.5 nm.